239 (2024) 212982

Contents lists available at ScienceDirect

Geoenergy Science and Engineering

journal homepage: www.sciencedirect.com/journal/geoenergy-science-and-engineering

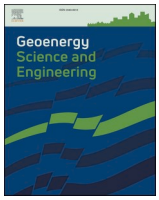

Augmenting X-ray micro-CT data with MICP data for high resolution pore-scale simulations of flow properties of carbonate rocks

Olubukola Ishola, Javier Vilcáez *

Boone Pickens School of Geology, Oklahoma State University, Stillwater, OK, 74078, USA

ARTICLE INFO

Keywords:
Pore-scale modelling
Stochastic pore connectivity
Carbonate rocks
Permeability
Tortuosity
Upscaling

ABSTRACT

Pore-scale modeling is essential in understanding and predicting flow and transport properties of rocks. Generally, pore-scale modeling is dependent on imaging technologies such as Micro Computed Tomography (micro-CT), which provides visual confirmation into the pore microstructures of rocks at a representative scale. However, this technique is limited in the ability to provide high resolution images showing the pore-throats connecting pore bodies. Pore scale simulations of flow and transport properties of rocks are generally done on a single 3D pore microstructure image. As such, the simulated properties are only representative of the simulated pore-scale rock volume. These are the technological and computational limitations which we address here by using a stochastic pore-scale simulation approach. This approach consists of constructing hundreds of 3D pore microstructures of the same pore size distribution and overall porosity but different pore connectivity. The construction of the 3D pore microstructures incorporates the use of Mercury Injection Capillary Pressure (MICP) data to account for pore throat size distribution, and micro-CT images to account for pore body size distribution. The approach requires a small micro-CT image volume (7–19 mm^3) to reveal key pore microstructural features that control flow and transport properties of highly heterogeneous rocks at the core-scale. Four carbonate rock samples were used to test the proposed approach. Permeability calculations from the introduced approach were validated by comparing laboratory measured permeability of rock cores and permeability estimated using five well-known core-scale empirical model equations. The results show that accounting for the stochastic connectivity of pores results in a probabilistic distribution of flow properties which can be used to upscale pore-scale simulated flow properties to the core-scale. The use of the introduced stochastic pore-scale simulation approach is more beneficial when there is a higher degree of heterogeneity in pore size distribution. This is shown to be the case with permeability and hydraulic tortuosity which are key controls of flow and transport processes in rocks.

1. Introduction

Appropriate information of the pore microstructure of rocks is crucial in many geoscience and engineering applications (Ishola et al., 2022; Regnet et al., 2019; Starnoni et al., 2017) such as hydrocarbon exploration (Ebrahimi and Vilcáez, 2019; Vilcáez, 2020), geothermal exploration, groundwater exploration, carbon sequestration (Shabani et al., 2020; Shabani and Vilcáez, 2019), hydrogen storage, mineral exploration, and environmental studies (Omar and Vilcáez, 2022). The pore microstructure of rocks control fundamental flow and transport properties of rocks such as permeability and hydraulic tortuosity (Ishola et al., 2022). The pore microstructure of rocks can be described as the configuration of voids. Characteristic features of pore microstructures include pore throats, pore body, pore shape, and pore topology. These features vary in rocks because of heterogeneity. Generally, pore microstructures are less heterogenous in sandstone and more heterogenous in carbonate rocks. Heterogeneity in natural rocks result largely from a combination of deposition and diagenesis processes (Hollis, 2011; Morad et al., 2010; Regnet et al., 2019; Wang et al., 2017). An increase in the degree of heterogeneity has been shown to lead to increased degree of uncertainty in permeability and hydraulic tortuosity of rocks (Ishola et al., 2022). Traditionally, flow properties such as permeability are predicted from macroscale petrophysical properties of rocks such as porosity. While this approaches generally work well in sandstone, they often fail in carbonate rocks because of the inherent heterogeneity (Dasgupta and Mukherjee, 2020; Westphal et al., 2005). A same porosity

* Corresponding author.
E-mail address: vilcaez@okstate.edu (J. Vilcáez).

https://doi.org/10.1016/j.geoen.2024.212982
Received 18 December 2023; Received in revised form 8 April 2024; Accepted 24 May 2024
Available online 25 May 2024

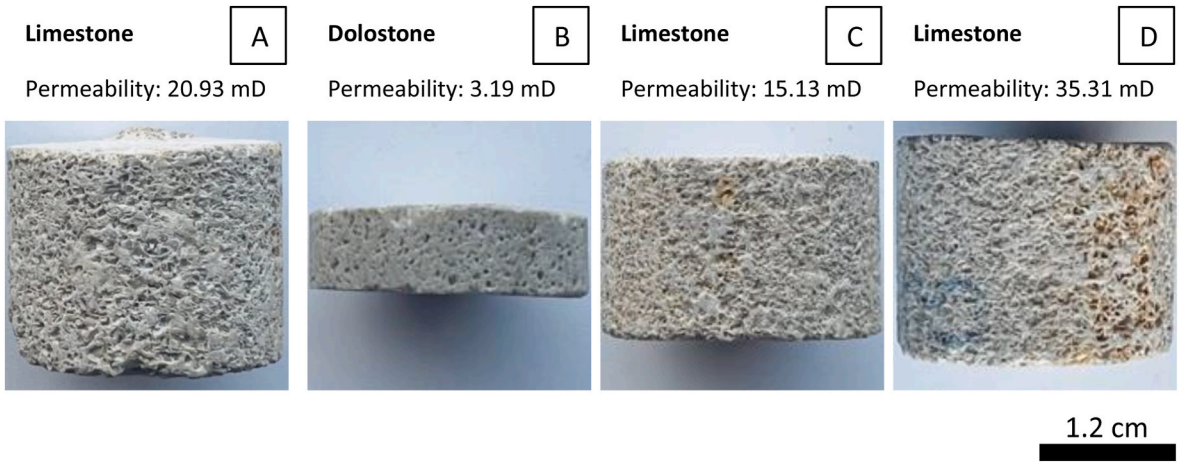

Fig. 1. Rock samples (A–D) used in this study along with respective permeability measured in each sample.

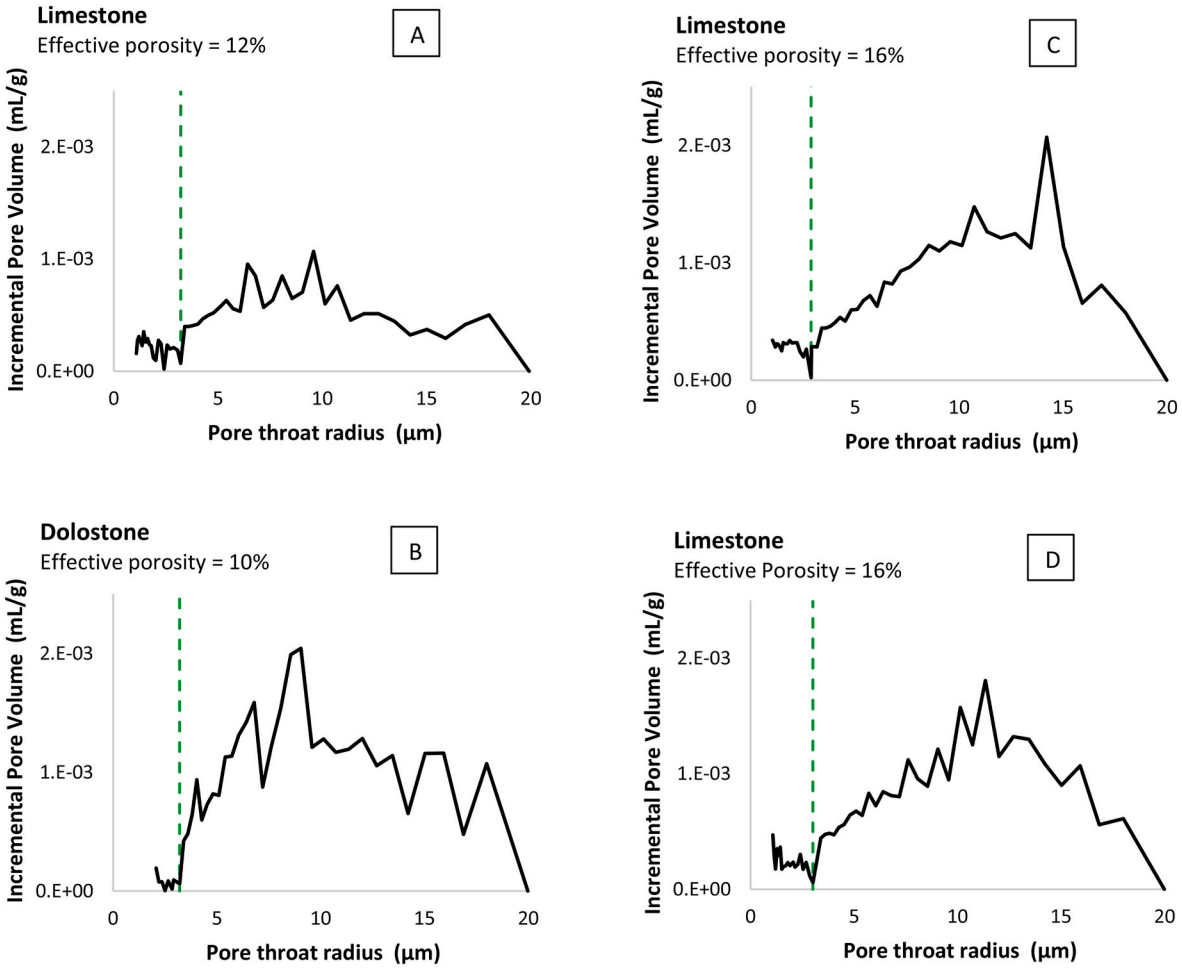

Fig. 2. MICP data of pore throat radius for study samples in Fig. 1. The dashed green line denotes the threshold below which data is considered unreliable.

Table 1
EPTR of rock samples used in this study.

Sample	A	B	C	D
EPTR (µm)	7.016	7.503	7.773	7.785

value has been shown can be associated to permeability values spanning five orders of magnitude if pore microstructural features such as pore size distribution and pore connectivity are not accounted for (Westphal et al., 2005; Yang and Aplin, 2010; Zhang et al., 2018). To help constrain this issue, pore size distribution data via measurements like nuclear magnetic resonance (NMR) (Westphal et al., 2005) and mercury injection capillary pressure (MICP) (Comisky et al., 2007) have been incorporated into empirical approaches to predicting permeability.

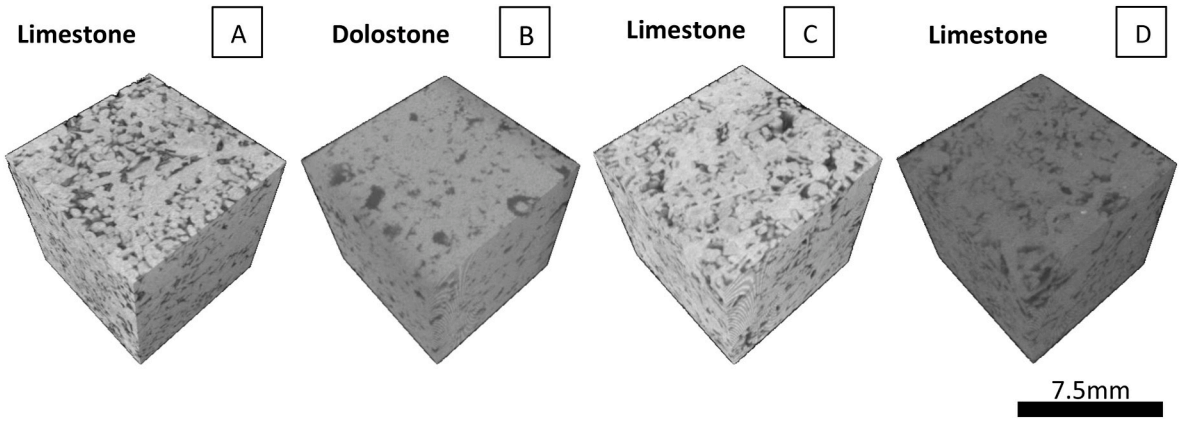

Fig. 3. 3D micro-CT images of the four carbonate samples (A–D) used in this study.

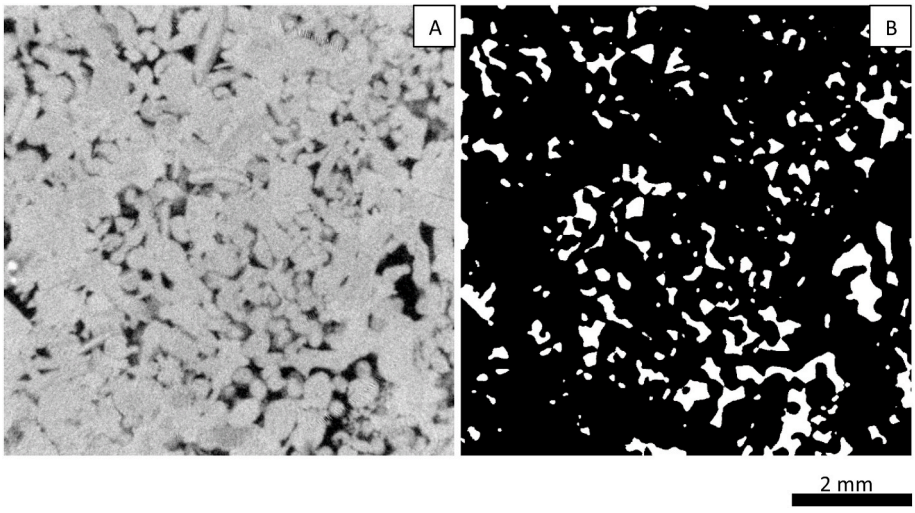

Fig. 4. (a) A 2D slice through unprocessed micro-CT image of sample A. (b) A 2D slice through segmented micro-CT image of sample A.

Conventionally, the inclusion of pore connectivity to predict permeability relies on 3D imaging techniques which are used to reveal the position of three-dimensional connections that exist between pores in rocks (Bernabé et al., 2010; Civan, 2002; Dasgupta and Mukherjee, 2020; Ishola et al., 2022). There are two main techniques for obtaining 3D images of rocks, namely the focussed ion beam scanning electron microscope imaging (FIB-SEM) and the X-ray computed tomography (micro-CT) techniques. The more common approach is the use of micro-CT technique (Bazaikin et al., 2017; Xiong et al., 2016; Zhang et al., 2019). The Micro-CT technique has the capacity to image relatively large volumes of rocks (typically, rock cores of 1-inch diameter by few inches length) such that the calculated rock properties are representative at continuum scale. That said, there is a linear relationship between sample size and resolution of images obtained from micro-CT (Bazaikin et al., 2017). This implies that obtaining high resolution images of rocks is only possible for smaller sample sizes which is at the cost of the representative nature of pore microstructural information obtained from the rock samples (Bazaikin et al., 2017; Blunt et al., 2013; Mees F. et al., 2003; Xiong et al., 2016). Conversely, a representative sample size has lower image resolution resulting in the erosion of smaller pore-throats and the associated pore connectivity. For a sample size ranging from ~0.5 to ~100 mm, the corresponding resolution of images obtainable ranges from ~0.7 to ~120 μm (Wang and Miller, 2020). Micro-CT technology often fail to capture the connecting paths in low permeability rocks at representative scale, resulting in 3D images of floating unconnected pores which is unsuitable for direct pore-scale simulation of fluid flow on the 3D pore microstructure image. Poor resolution of micro-CT images could also lump unresolved pore microstructures with larger ones resulting in higher average pore-microstructural features which can significantly increase permeability (Devarapalli et al., 2017). In agreement to the observations of Devarapalli and others, Saxena et al. (2018) and others showed the lower limit of permeability for a given porosity to increase with coarser resolution of micro-CT images due to the overestimation of pore-throat sizes in the micro-CT images (Saxena et al., 2018; Uchic et al., 2007). This indicates the crucial role of resolution in predicting flow properties of heterogeneous rocks from rock micro-CT images. It is noteworthy that the accuracy of flow property estimations derived from rock images can also be influenced by the type of numerical model applied, the boundary conditions set during simulation, and how precisely the pore spaces are distinguished from the solid material in the image segmentation process (Khirevich et al., 2015; Reinhardt et al., 2022). The main technique to obtaining high resolution images of rock samples is by using FIB-SEM (Blunt et al., 2013; Uchic et al., 2007; Vilcáez et al., 2017; Xiong et al., 2016) which is a destructive technique that provides image resolution of up to 0.4 nm but can only image up to tens of cubic microns of the rock sample which is not statistically representative of heterogeneous rocks. Statistically representative volume of heterogeneous rock varies from study to study (Saraji and Piri, 2015; Uchic et al., 2007; Vilcáez et al., 2017; Xiong et al., 2016). High resolution images from micro-CT and FIB-SEM approaches comes at the cost of sample size (Saxena et al., 2018) and this is more consequential with higher

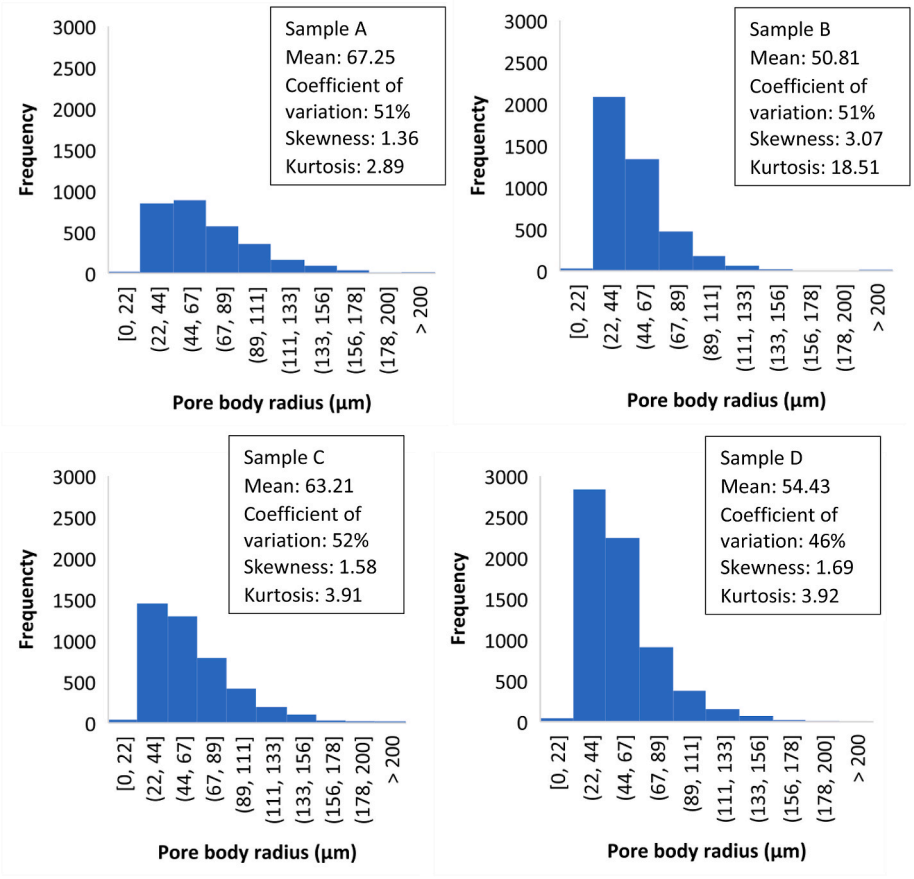

Fig. 5. Pore size distribution (PSD) of all samples micro-CT images (Fig. 3).

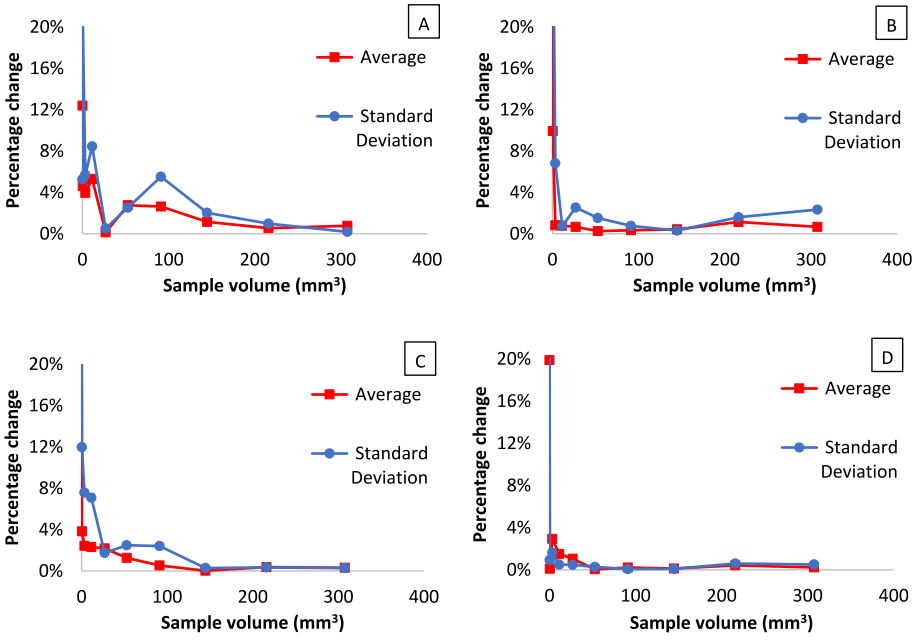

Fig. 6. Percentage changes in average and standard deviation of PSD. (A)–(D) corresponds to rock samples A, B, C, and D. The micro-CT images of the rock samples (Fig. 3) were obtained using Phoenix Nanotom M at Baker Hughes facility in Oklahoma City, USA.

heterogeneity. This is because the volume to reach the representative elementary volume (REV) will often get larger as heterogeneity increases (Adeleye and Akanji, 2018; Bear, 1972; Ghanbarian, 2022; Sadeghnejad et al., 2023). Hence, for relatively homogenous samples, smaller sample sizes might suffice, allowing the acquisition of high-resolution images that are representative in nature.

There are several approaches to accounting for pore connectivity in images with poor resolution. This includes the use of random

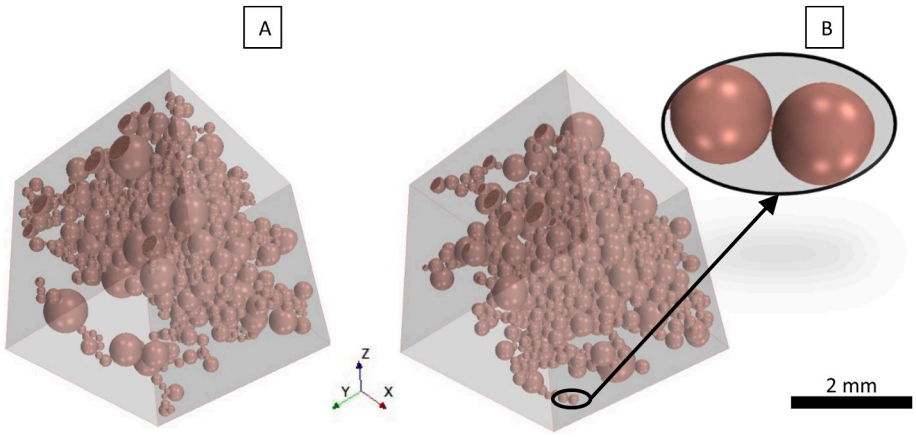

Fig. 7. (a) and (b) show two stochastic pore-microstructural models of sample D. (b) is zoomed in to reveal the pore throat pore body relationship.

Table 2
General properties of 200 stochastically generated 3D pore-microstructures.

Sample	Minimum number of pores	Maximum number of pores	Average digital rock volume (mm^3)	Minimum digital rock volume (mm^3)	Maximum digital rock volume (mm^3)
A	950	997	19.18	16.21	25.44
B	950	1000	11.11	8.51	16.49
C	953	998	12.76	10.60	15.10
D	951	998	7.16	6.07	8.61

distribution of pore connectivity to account for possible connectivity scenarios (Jivkov et al., 2013; Jivkov and Xiong, 2014). However, the approach by Jivkov et al. (2013) and others assumes uniform spatial distribution of pore centroids which is not the case in heterogenous rocks. Mehmani and Prodanovic' (2014) approached pore network modelling differently by using the Delaunay tessellation of grain centres in a two-scale network construction. The workflow yielded less structured spatial distribution but assumes a fixed connectivity with a coordination number of four in its macronetwork and micronetwork (Mehmani and Prodanović, 2014). The fixed nature of pore connectivity is the key limit of this approach as this is not a feasible configuration for heterogeneous rocks. Statistical approaches such as multiple-point statistics (Okabe and Blunt, 2004) have been shown to reproduce realistic pore microstructural information of 2D thin sections of rocks which in turn produced reasonable permeability values. Wu et al. (2018) and others improved on this approach by using 3D micro-CT images in their reconstruction which accounts for anisotropy and 3D configuration of the pore microstructure. Like the approaches led by Jikov et al. (2013), Mehmani and Prodanović (2014), and Okabe and Blunt (2004), the capacity of 3D multipoint statistics to capture and produce realistic pore connectivity depends on the quality of the image in terms of resolution and its statistical representation of the rock sample. Furthermore, the proposed workflow by Wu et al. (2018) and others does not work well with high heterogeneity. In recent literature, innovative approaches to pore network modelling have been utilized for varying problems. This includes the use of a novel graph-based method to address the phase connectivity problem within the context of simulating capillary-driven

Table 3
Statistics of cell count across generated pore-microstructural models.

Sample	Average	Minimum	Maximum
A	5,602,059	4,035,754	6,141,038
B	3,778,544	3,050,166	4,160,014
C	4,618,266	3,888,282	4,843,624
D	4,146,574	3,301,447	4,335,784

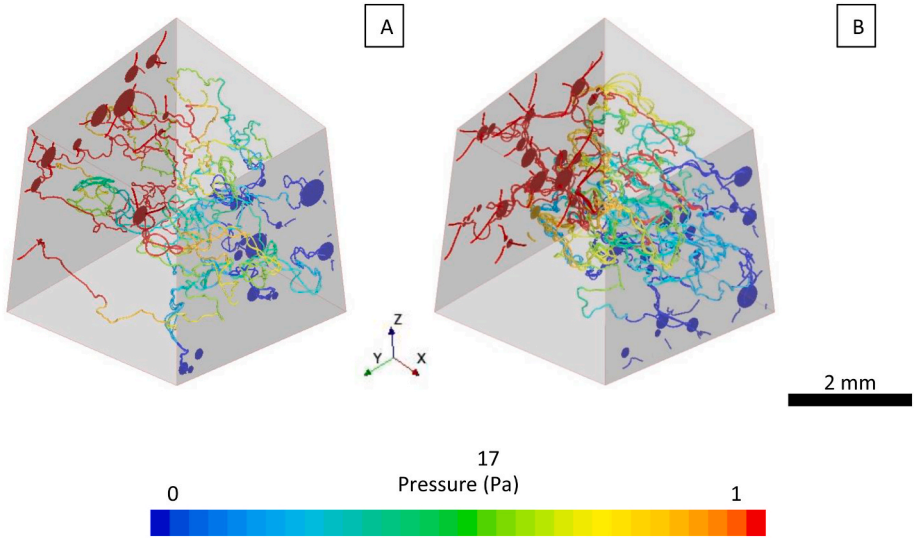

Fig. 8. Pressure distribution superimposed on principal flow paths through the pore-microstructural models in Fig. 7 at steady state. Flow in the image is in the positive X direction.

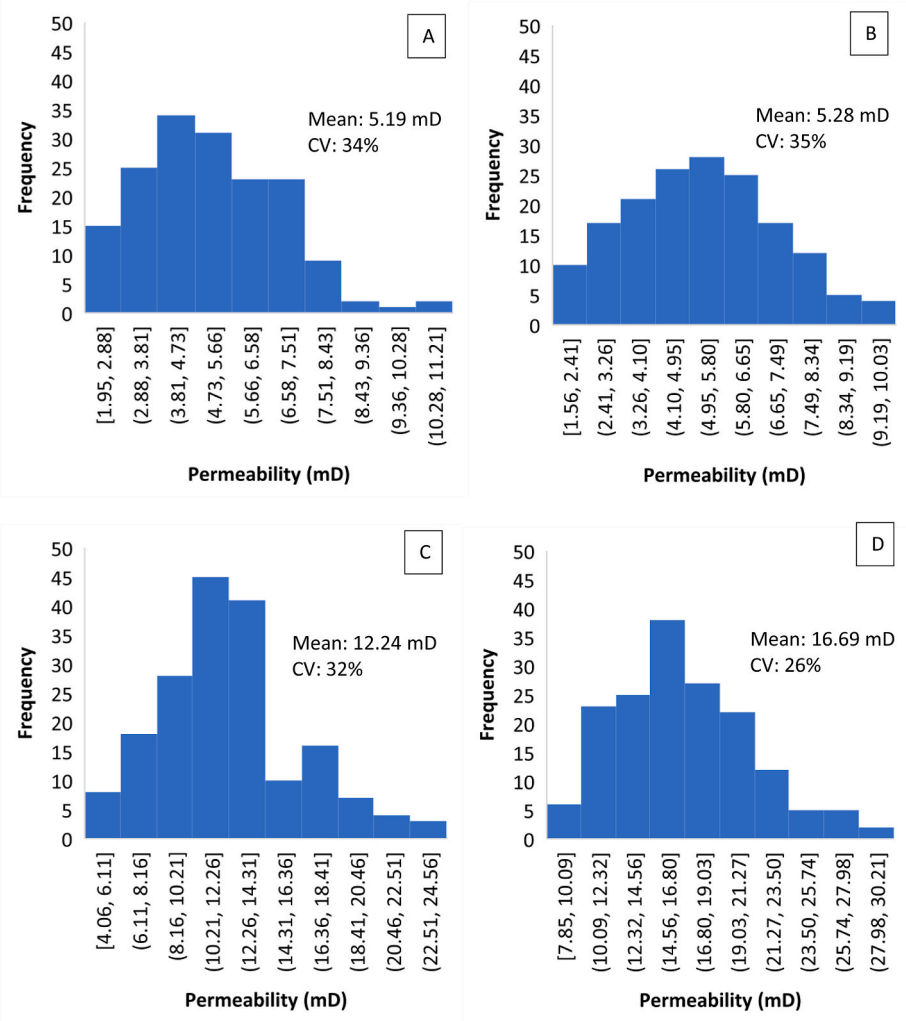

Fig. 9. Permeability distribution across respective samples.

immiscible displacement in permeable media (Petrovskyy et al., 2021). Additionally, a study by Moslemipour and Sadeghnejad (2021) has developed and applied a dual-scale Pore Network Model (PNM) to effectively capture and simulate the complex multiscale pore structure characteristic of vuggy carbonate rocks, which are notably challenging. This model efficiently preserves the connectivity between vugs and pores, even when they overlap. The results demonstrate that the reconstructed dual-scale PNM closely matches the laboratory measurement data of the actual rock sample.

In an earlier study (Ishola et al., 2022), we emphasize the relevance of accounting for the stochastic connectivity of pores in making predictions of permeability and hydraulic tortuosity of heterogeneous porous media by using equally probable stochastic pore connectivity scenarios where porosity and pore size distribution are kept constant. The approach in that study replicates permeability pattern found in real rocks which is validated by the lognormal distribution of permeability found in real heterogenous rocks (Malin et al., 2020; Sahin et al., 2007). In another study (Ishola and Vilcáez, 2022), we applied the proposed stochastic pore-scale simulation approach to predict permeability of nine rocks. Generally, the estimated permeability of the samples was closer to true values when compared to five popular empirical permeability equations. In the current study, we built on our existing workflow (Ishola et al., 2022; Ishola and Vilcáez, 2022) to generate realistic pore microstructures by augmenting X-ray micro-CT data with MICP data to account for a wider range of pore sizes and pore connectivity. This novel workflow uses high resolution and statistically representative data simultaneously. Here, we estimate an effective pore throat radius (EPTR) from MICP data while the distribution of pore body radius (PSD) was obtained from micro-CT images. Like other studies, we simplified the pore shape to a sphere of equivalent volume to the true geometry. To account for pore connectivity, we employed the stochastic approach by (Ishola et al., 2022; Ishola and Vilcáez, 2022) to generate equally probable stochastic pore connectivities in rock samples of the same porosity and pore size distribution. The results of this approach are validated by comparing the simulated permeabilities by this new approach to laboratory measured permeability values as well as to estimated permeability values from well-known empirical permeability models.

2. Material and methods

Four carbonate rock samples were used in this study (Fig. 1). For each of the rock samples three sets of data were obtained. This includes laboratory permeability measurement of the samples (Section 2.1), MICP information (Section 2.2), and 3D micro-CT images (Section 2.3).

2.1. Experimental rock permeability

Permeability of our samples were obtained using Darcy's law (Darcy, 1856) via Eq. (1).

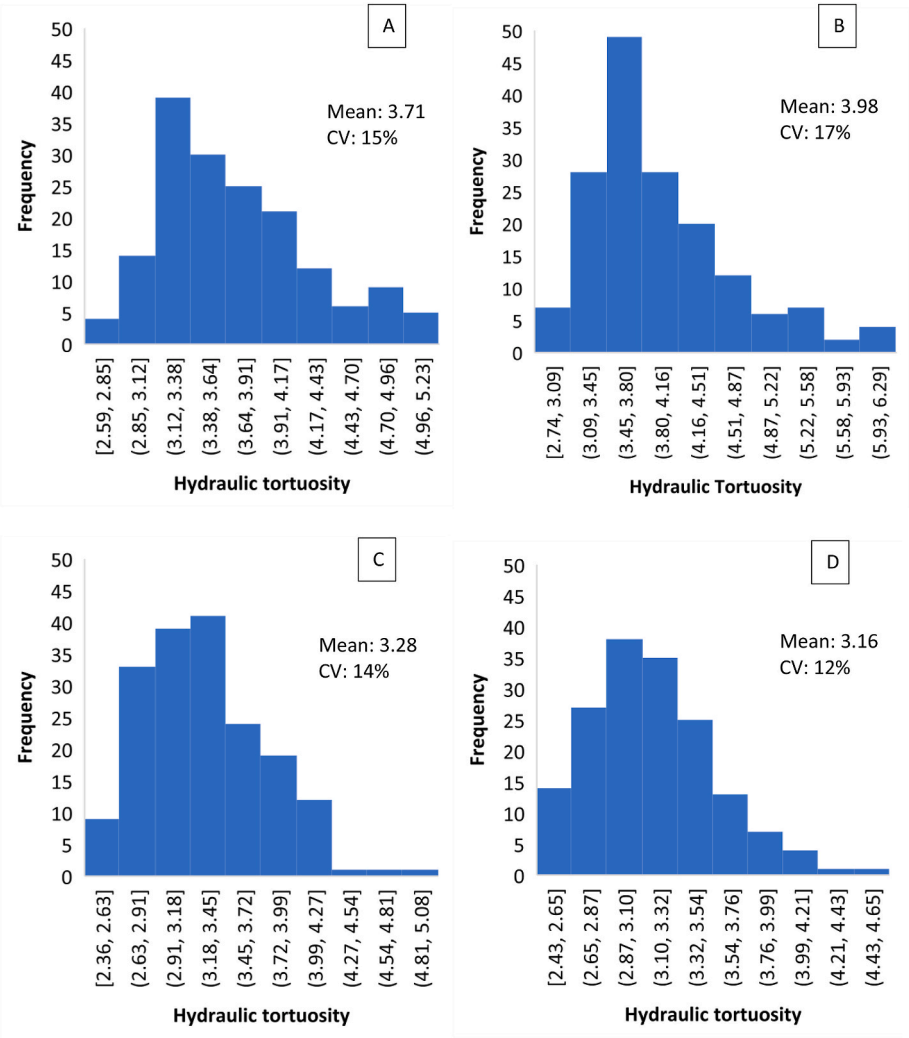

Fig. 10. Hydraulic tortuosity distribution across respective samples.

$$K = \frac{Q \times \mu \times L}{A \times \Delta P} \quad (1)$$

where K is the absolute permeability of the rock domain (m^2), Q is the volumetric flowrate through the rock sample (m^3/s), μ is the dynamic viscosity of the fluid injected into the rock sample (Pa-s), L is the length along the principal direction of fluid travel in the rock sample (m), A is the cross-sectional area of flow (m^2), and ΔP is the pressure drop in the principal direction of the fluid flow (Pa).

In our laboratory setup for permeability measurement, we used a Hassler Type core-holder (RCH-series of Core Laboratory) to hold the rock samples at a pressure of 2000 psi. Water was injected into the held rock samples with a 260 dual syringe pump (Teledyne ISCO) at flow rates ranging from 0.025 to 0.5 ml/min. The range of flow rate used in this study resulted in a maximum Reynolds number of 1×10^{-4} which ensures that the application of Darcy's laws to estimate permeability is valid in all our laboratory measurements. We used a Rosemount Pressure Sensor to measure pressure at the inlet of our samples while the outlet pressure is known to be atmospheric pressure for our experimental setup. The experiment is deemed to have reached steady state when the pressure drops across the sample stopped changing through time.

2.2. Effective pore throat radius

In this study, to help capture the resultant effect of pore throats on the permeability of heterogeneous rocks, we incorporate pore throats of an effective pore throat radius (EPTR) into our approach to construct pore microstructures of the same porosity, pore body size distribution, but stochastic pore connectivity (Ishola et al., 2022; Ishola and Vilcáez, 2022). EPTR in this study refers to the weighted average pore throat size, estimated from MICP data (Fig. 2). This is an improvement from previous studies where pore throats were inferred from micro-CT images (Sun et al., 2021; Willson et al., 2012; Zhang et al., 2022) which has poor resolution for representative volumes required to represent rock samples (Bazaikin et al., 2017; Blunt et al., 2013; Mees F. et al., 2003; Xiong et al., 2016). We estimated EPTR from MICP data of rock sample at continuum scale via three steps:

Step one: Account for the ink bottle effect. The pore shadowing or ink-bottle phenomenon (Xiong et al., 2016) can lead to an overestimation of smaller pore sizes during MICP data acquisition. This is because of the increase in pressure from mercury injection obscures the presence of larger pore volumes located beyond narrower pores, mistakenly categorizing them as tight pores. To address the ink bottle effect, we used a cutoff at points indicated by a dashed green line in Fig. 2, where the incremental pore volume approaches zero, followed by a pronounced increase. These minimal incremental pore volumes likely contribute to the ink bottle effect by hindering the flow of mercury during the injection process. Additionally, the sharp increase across the cutoff line suggests that the pore throats on either side of this line have limited interaction. It is critical to note that by setting this threshold, we

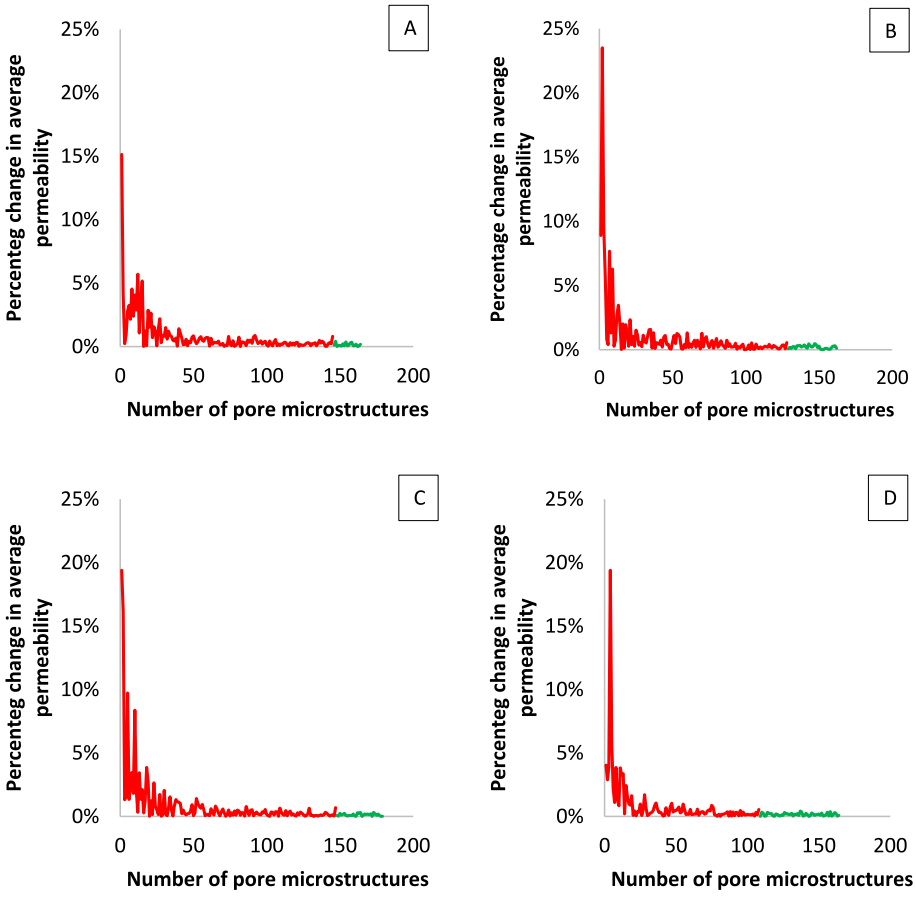

Fig. 11. Percentage change in average permeability with number of pore-scale simulated permeability. Red portion of the plot is deemed unrepresentative while green is deemed representative. Representative number of pore microstructures used to simulate permeability for (a) is 144, (b) is 128, (c) is 146, and (d) is 108.

also disregard any genuine pores that are smaller than this threshold. However, Fig. 2 demonstrates that the pore throats below this threshold account for a negligible portion of the total pore volume. Therefore, this method offers a favorable balance when attempting to minimize the impact of the ink bottle effect on our EPTR calculations.

Step two: Estimate the weight of each pore throat size. In a previous work by Dastidar et al. (2007) the fraction of each incremental pore volume is used as weights Eq. (2):

$$w_i = \frac{v_i}{\sum_{i=1}^{n} (v_i)} \tag{2}$$

where n is the number of pore throat size data points, and v_i is the incremental pore volume of a given pore throat i. Here, we used the ratio of the incremental pore volume to the curved surface area (s) of an equivalent cylinder as weights:

$$w_i = \frac{v_i/s_i}{\sum_{i=1}^{n} (v_i/s_i)} \tag{3}$$

curved surface area (s) is given by:

$$s_i = 2\pi r_i h_i \tag{4}$$

where r_i is the radius of a given pore throat i and h_i is the corresponding pore throat length. In this study we assumed h_i to be constant, hence, s_i is controlled by r_i in Eq. (3). The incremental pore volume (v_i) accounts for the fraction of total volume of fluid a pore throat (i) controls. The curved surface area s_i is introduced in this study to account for the impact of frictional interaction at the fluid-rock interface which negates flow through a pore throat i. Curved surface area and not total surface area is used here because the pore throats are idealized as cylinders and the portion of the cylinder having the frictional interaction with the fluid flowing through is the curved surface since the idealized cylinder is expected to be hollow for fluid to pass through it.

Step three: Calculate the EPTR by using the estimated weights to compute a weighted average pore throat radius (Eq. (5)).

$$EPTR = \frac{\sum_{i=1}^{n} (w_i \times r_i)}{\sum_{i=1}^{n} (w_i)} \tag{5}$$

The estimated EPTR (Table 1) was used as the pore throat radius to construct 3D pore microstructures following our stochastic approach (Ishola et al., 2022; Ishola and Vilcáez, 2022). The MICP data also provided effective total porosity which was used as control to constrain constructed pore microstructures.

The MICP data of the samples (Fig. 2) were obtained from Integrated Core Characterization Center, University of Oklahoma, USA.

2.3. Pore body size distribution (PSD) data

The PSD used in this study was obtained from micro-CT images of the rock samples in Fig. 1. It is noteworthy that micro-CT imaging is the chosen approach for obtaining PSD ahead of other methods because it captures 3D visual representation of pores present in each of the samples and is a much more scalable and non-destructive option of obtaining the true pore microstructures in rocks, albeit, at lower resolution compared to some approaches. The size of the micro-CT images for all the samples is 1000 x 1000 x 1000 pixels in x, y, and z directions with a resolution of

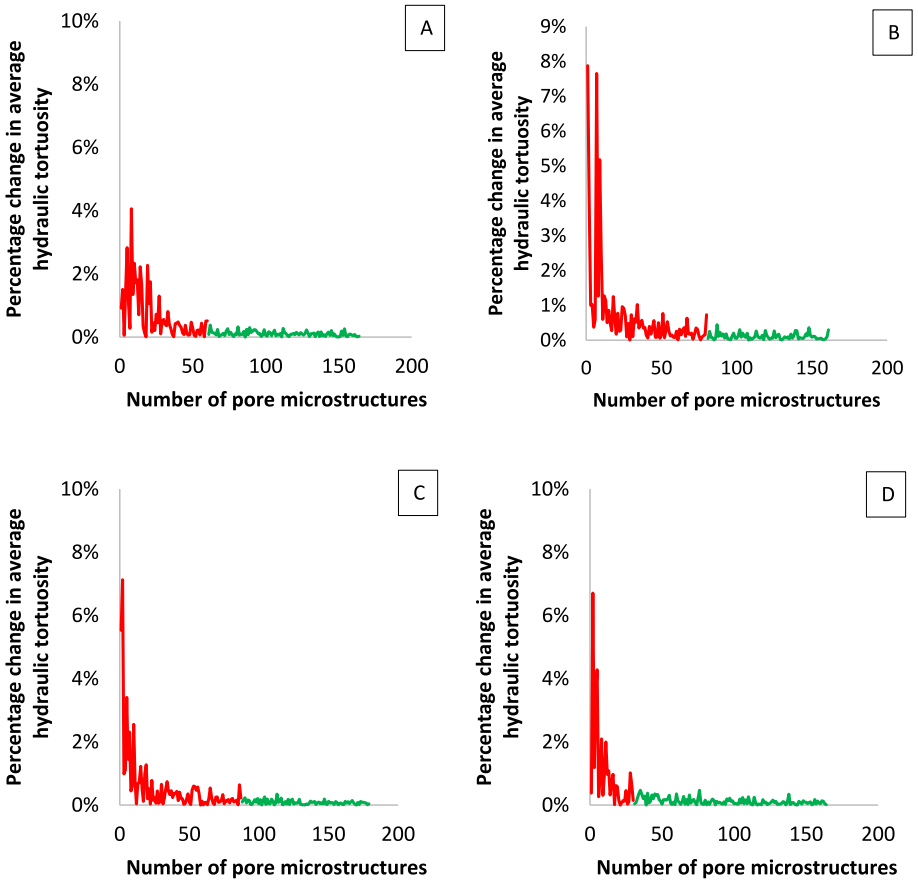

Fig. 12. Percentage change in average hydraulic tortuosity with pore-scale simulated hydraulic tortuosity. Red portion of the plot is deemed unrepresentative while green is deemed representative. Representative number of pore microstructures used to simulate hydraulic conductivity for (a) is 61, (b) is 80, (c) is 88, and (d) is 31.

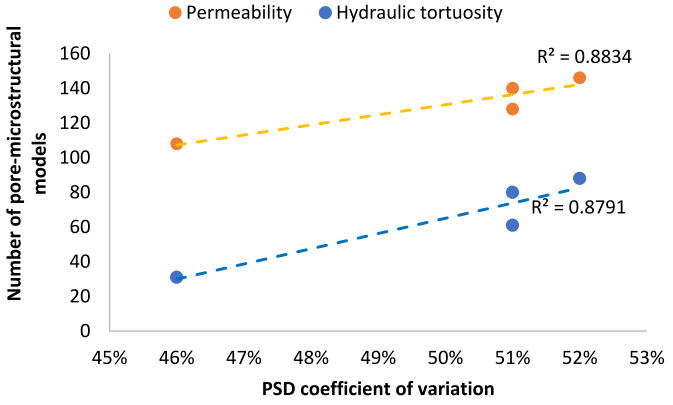

Fig. 13. Relationship between heterogeneity (PSD coefficient of variation) and required number of pore-microstructures to obtain representative nature of observed flow properties.

7.5 μm (Fig. 3). The resulting 422 mm^3 volumes were segmented (Fig. 4.) to separate the pores in the image from the background using a watershed algorithm.

The watershed algorithm (Gostick, 2017) was used to prevent overestimation of pore volumes via the separation of pores connected in the images. The volume distribution of the resultant isolated pores was obtained from the segmented image. PSD (Fig. 5) is obtained from the volume distribution by calculating the pore radius of equivalent spherical volume for each of the pores (Eq. (6)).

Table 4
Permeability measurements/estimations using different approaches.

Permeability model approach	Sample A (mD)	Sample B (mD)	Sample C (mD)	Sample D (mD)
Experimental permeability	20.96	3.19	15.13	35.31
Winland (Kolodzie, 1980a, b)	9.29	68.75	46.16	40.51
Swanson (Swanson, 1981)	12.68	55.93	42.19	40.02
Wells-Amaefule Method (Wells and Amaefule, 1985)	2.28	7.24	5.82	5.58
Kamath Method (Kamath, 1992)	24.29	79.41	63.41	60.8
OU Method (Dastidar et al., 2007)	5.22	36.49	12.24	12.14
Current study	5.19	5.28	12.24	16.69

$$R_i = \sqrt[3]{\frac{3 \times V_i}{4 \times \pi}} \quad (6)$$

where R_i is the radius of the equivalent sphere of volume V_i and i is the pore obtained from the micro-CT image.

To verify the representative nature of the PSD data, we conducted a representative elementary volume (REV) analysis on the segmented 3D image for each sample (Bear, 1972). The purpose of the REV analysis was to determine if the PSD obtained from the micro-CT data is representative. In the REV analysis, we evaluated the percentage change in average PSD, and standard deviation of PSD (Fig. 6) for subvolumes of micro-CT image data (Fig. 4), ranging from 0.05 mm^3 to 422 mm^3. For this study, a 5% change in average pore-size was applied as cut off for

Table 5
Mean absolute percentage error (MAPE) of current study compared to five other approaches to estimating permeability.

Permeability model approach	Percentage error				MAPE (%)
	Sample A (%)	Sample B (%)	Sample C (%)	Sample D (%)	
Winland (Kolodzie, 1980)	56	2055	205	15	583
Swanson (Swanson, 1981)	40	1653	179	13	471
Wells-Amaefule Method (Wells and Amaefule, 1985)	89	127	62	84	90
Kamath Method (Kamath, 1992)	16	2389	319	72	699
OU Method (Dastidar et al., 2007)	75	1044	19	66	301
Current study	75	66	19	53	53

the representative volume. The REV analysis showed all our samples to have a representative volume of 27 mm^3 given by the relatively low percentage change in all the three statistical parameters tracked through the varying volume of the rock images (Fig. 6). This implies that any subsample in the range of 27 mm^3–422 mm^3 will approximately have the same PSD.

2.4. Stochastic generation of 3D pore microstructures

In this study, we employ our stochastics approach (Ishola and Vilcáez, 2022) to generate 3D pore microstructures of the same pore size distribution and effective porosity but different pore connectivity. In this study we assumed a cylindrical pore throat with length of 1 μm. The radius of the pore throats (EPTR) was estimated from MICP data as described in section 2.2. The pore sizes were randomly obtained from the respective PSDs of the samples and the pore throat sizes were fixed to the respective EPTRs. The pore microstructures construction approach involves the stochastic spatial distribution of pores in a computational domain given four constraints. The first constraint is that the first pore in the computational domain is at the centre to allow equal possible spreading path to the entire domain. Subsequent connections start randomly along established paths in the computational domain. The second is that a space already occupied by a pore is no longer available to subsequent pores added into the system. The third constraint is that for a pore microstructure to be valid, there must be at least a connecting path between the inlet and outlet of the computational domain. The fourth constraint is that porosity is equal to effective porosity, and this is provided by the MICP data in this study. The resultant stochastic 3D pore microstructure has equal probability of occurring while honouring the effective porosity and pore size distribution of the parent sample (Fig. 7). The number of pores in each 3D pore microstructures in this study ranges from 950 to 1000 which consequently results in 3D pore microstructural volumes ranging from 6.07 to 25.44 mm^3 (Table 2). It is noteworthy that the volume of the 3D pore microstructure varies depending on the number of pores (Table 2), sizes of the pores sampled from the PSD (Fig. 5), and the effective porosity of the sample (Fig. 2).

2.5. Direct pore-scale simulations of permeability

Permeability of the 3D pore microstructures (Fig. 7) was estimated from Eq. (1) using data obtained from pore-scale simulations of fluid flow. For each rock sample, 200 pore microstructures were generated and used for flow simulation. Steady state simulations of fluid flow (Fig. 8) were accomplished with STAR-CCM+®, a computational fluid dynamics software that solves the mass continuity equation (Eq. 7) and Navier Stokes equation (Eq. 8) using its finite volume methodology.

$$\vec{\nabla}\cdot\rho\vec{V}+\frac{\partial\rho}{\partial t}=0 \tag{7}$$

$$\frac{\partial\vec{V}}{\partial t}+\left(\vec{V}\cdot\vec{\nabla}\right)\vec{V}=-\frac{1}{\rho}\vec{\nabla}P+\nu\vec{\nabla}^2\vec{V} \tag{8}$$

where ρ is density of the fluid, ν is kinematic viscosity, P is pressure, t is time, and $\vec{V}$ is fluid velocity.

STAR-CCM+® has been benchmarked against experiments and shown to accurately replicate pore scale fluid flow (Oostrom et al., 2016; Yang et al., 2013, 2016). In this study, we used an unstructured polyhedral mesh type to capture the complex geometry of the 3D pore-microstructural models generated. All the generated 3D pore microstructures were assigned a minimum cell size of 0.2 μm while other parameters in the mesh generator were kept at default. The number of cells in each pore microstructure varied from 3,050,166 to 6,141,038 (Table 3).

In all simulations, water was used as the fluid and there was no chemical reaction in the computational domain. A no-slip wall boundary condition was used throughout the computational domain except at the opposite sides along the intended flow direction which had inlet pressure set at 1 Pa and outlet pressure set at 0 Pa to drive fluid flow. To ensure that permeability calculations were valid, we made certain that the Reynolds number of all the pore scale simulations was less than 1 since Darcy's law (Darcy, 1856) was used in estimating permeability (Eq. (1)). All simulations were seen to have converged for permeability when the change in permeability in the last two iterations is less than 1% while attaining residuals (continuity, x momentum, y momentum, and z momentum) were less than 10^{-4} by the end of 200 iterations assigned in all our flow simulations.

2.5.1. Permeability estimations from empirical models

To evaluate if augmenting X-ray micro-CT data with MICP data produces realistic 3D pore microstructures and thus permeability values using our previously proposed stochastic pore-scale simulation approach, the arithmetic average permeability of 200 possible pore microstructures was compared with experimental permeability values as well as with permeability values estimated from popular empirical models. Empirical models considered includes Winland (Kolodzie, 1980), Swanson (Swanson, 1981), Wells-Amaefule (J.D. Wells and Amaefule, 1985, Kamath, 1992), and Dastidar (Dastidar et al., 2007) models given by Eqs. (9)–(13).

$$k_{Winland}=49.4*R_{35}^{1.7}*\varnothing^{1.47} \tag{9}$$

$$k_{Swanson-brine}=355*\left[\frac{s_b}{P_C}\right]_A^{2.005} \tag{10}$$

$$k_{Wells-Amaefule}=30.5*\left[\frac{s_b}{P_C}\right]_A^{1.56} \tag{11}$$

$$k_{Kamath}=347*\left[\frac{s_b}{P_C}\right]_A^{1.60} \tag{12}$$

$$k_{Dastidar}=4073*R_{wgm}^{1.64}*\varnothing^{3.06} \tag{13}$$

where s_b is the percent bulk volume occupied by mercury, P_C is the mercury capillary pressure (psia), A is the maximum amplitude, R_{35} is 35% mercury saturation of pore volume, $\varnothing$ is porosity (fraction), and R_{wgm} is the geometric mean of pore sizes.

3. Results and discussion

3.1. Role of stochastic pore connectivity

In this study, we evaluated the importance of pore connectivity on estimating flow properties (permeability and hydraulic tortuosity) of heterogeneous rocks using fluid flow simulations on stochastically generated 3D pore-microstructures for four rock samples. Different from the traditional approach where flow properties are simulated using a single micro-CT image assuming an arbitrary pore connectivity due to the inability of micro-CT to capture small pore throats, here we construct hundreds of 3D pore microstructures of stochastic pore connectivity and equal probability of occurrence using PSD data from micro-CT data and pore throat radius data inferred from MICP data. As such, this approach does not only solve the problem of low resolution of micro-CT images to capture pore connectivity, but it also accounts for the effect of the stochastic nature of pore connectivities in rocks. Each sample of given PSD, shows a permeability distribution (Fig. 9) with a coefficient of variation of 34% in sample A, 35% in sample B, 32% in sample C, and 26% in sample D. The variation in permeability (Fig. 9) in all samples confirms the relevance of accounting for the stochastic connectivity of pores in estimating the flow properties of heterogeneous rocks. The same applies to hydraulic tortuosity which is shown in Fig. 10 to have a coefficient of variation of 15% in sample A, 17% in sample B, 14% in sample C, and 12% in sample D. Given that pore connectivity cannot be measured directly in rocks due to limitations in resolution and/or due to high cost, stochastically constructed 3D pore microstructures of equal probability of occurrence helps account for the unknown connectivity in rock samples. Considering the large number of possible connectivity scenarios reflected by a distribution of possible property (permeability and hydraulic tortuosity) values can be used to make more robust inferences. In this study, we obtain permeability and hydraulic tortuosity of the four samples by computing average permeability (Fig. 11) and hydraulic tortuosity (Fig. 12) values. The number of 3D pore microstructures and corresponding pore-scale simulated permeability and hydraulic tortuosity values used to calculate average permeability and hydraulic tortuosity values was deemed sufficient when the percentage change in permeability and hydraulic tortuosity values is approximately zero percent. As shown in Fig. 11, the number of required pore-scale simulations for permeability is 144 for sample A, 128 for sample B, 146 for sample C, and 108 for sample D. For hydraulic tortuosity, the number of required pore-scale simulations to be representative is 61 for sample A, 80 for sample B, 88 for sample C, and 31 for sample D (Fig. 12). The number of 3D pore microstructures and corresponding pore-scale simulations were lower for hydraulic tortuosity than for permeability. This is attributed to the lower influence of pore throat sizes and pore connectivity on hydraulic connectivity than on permeability (Ishola et al., 2022). This is also reflected by lower CV of hydraulic tortuosity obtained in this study (Fig. 10) compared to permeability (Fig. 9). A plot of number of 3D pore microstructures to reach REV against heterogeneity in the four samples (Fig. 13) show that the number of 3D pore microstructures required to obtain representative permeability and hydraulic tortuosity increases with heterogeneity. This implies that relatively heterogenous rocks benefits more from our stochastic pore-scale simulation approach.

3.2. Validation

To validate if augmenting X-ray micro-CT data with MICP data reproduced measured permeability of real heterogenous rock samples, we compared simulated permeability with measured permeability as well as permeability estimates from five well known model equations. We evaluated how close the estimated permeability from our approach and permeability estimates from the five model equations match the measured permeability of the four samples using mean absolute percentage error (MAPE). MAPE is given by $MAPE = \frac{1}{n}\sum_{i=1}^{n}\left|\frac{k_{m,i}-k_{e,i}}{k_{m,i}}\right| \times 100$ where $k_{m,i}$, and $k_{e,i}$ is the measured permeability and estimated permeability of respective samples while n is the total number of samples which is four in this study. Based on MAPE (Tables 4 and 5), the estimated permeability from our approach here matches more closely with measured values than the five empirical models considered in this study. From the MAPE calculated, we can interpret estimated permeability from our approach to generally differ from measured value by 53%. The closest MAPE to our result is the estimate obtained from using the Wells-Amaefule method which had an MAPE of 90% while the remainder of the empirical models have MAPEs greater than 300%. The comparative accuracy obtained by augmenting X-ray micro-CT data with MICP data shows that accounting for the stochastic connectivity of pores and actual pore throats, outperforms empirical models in predicting permeability. This validates the workflow introduced in this study where we account for the stochastic connectivity of pore bodies through pore throats via a combination of EPTR from MICP data, PSD from micro-CT images, and pore connectivity from stochastic modelling. There are at least two ways to reduce MAPE of the current study. This includes, (1) developing efficient codes that allows easy incorporation of the true pore shapes found in micro-CT images which like most studies is approximated to spheres in this study, and (2) obtaining super higher resolution images of the samples at representative scale beyond the micro-CT resolution of 7.5 μm in this study. Solving these problems will push constructed 3D pore microstructures closer to the truth. The use of real pore shapes is important to make our workflow viable for multiphase flows.

4. Conclusions

In this study, we augmented **pore size distribution data obtained from X-ray micro-CT images with pore throat size data obtained from MICP measurements for stochastically constructing high resolution 3D pore microstructures of the same porosity and pore size distribution but different stochastic pore connectivity**. The micro-CT and MICP data used to construct our 3D pore microstructures were obtained at continuum scale and covers a significant spectrum of pore microstructural features of interest. We showed that accounting for the stochastic connectivity of pores can result in a probabilistic distribution of flow properties of rocks which guides different possible outcomes that should be considered when upscaling pore-scale simulated flow properties to the core-scale and beyond. The use of the introduced stochastic pore-scale simulation approach is shown here to be more beneficial when there is a higher degree of heterogeneity in PSD. This is shown to be the case of permeability and hydraulic tortuosity which are key controls of transport processes in rocks. We validated the introduced stochastic pore-scale simulation approach by showing that the average simulated permeability values by the introduced stochastic pore-scale simulation match more closely with experimental core-scale measured permeability values in comparison to five well known empirical models. It is noteworthy that this study is based on single phase flow. To capture key interactions in multiphase flow, we suggest the use of angular or irregular pores instead of spherical pores. Our workflow will help build geological models that will better account for pore-scale factors in fluid flow as well as reactive transport processes simulations at the core- and field-scale levels. Key areas of application for this workflow includes petroleum production, carbon and hydrogen sequestration, environmental studies, and groundwater resources development.

Funding

This work was supported by the National Science Foundation under Grant HS-2041648.

CRediT authorship contribution statement

Olubukola Ishola: Writing – original draft, Software, Methodology, Investigation. **Javier Vilcáez:** Writing – review & editing, Methodology, Funding acquisition, Conceptualization.

Declaration of competing interest

The authors declare the following financial interests/personal relationships which may be considered as potential competing interests: Javier Vilcaez reports financial support was provided by National Science Foundation. If there are other authors, they declare that they have no known competing financial interests or personal relationships that could have appeared to influence the work reported in this paper.

Data availability

No data was used for the research described in the article.

Acknowledgments

We appreciate the Association of Petroleum Geologist Foundation (AAPG), Oklahoma Geological Foundation (OGF), and the Oklahoma City Section of Society of Petroleum Engineers (SPE) for partial financial support of the Ph.D. research of the first author. This is Oklahoma State University Boone Pickens School of Geology contribution number 2024-141. Some of the computing for this project was performed at the High-Performance Computing Center at Oklahoma State University (OSU).

References

Adeleye, J.O., Akanji, L.T., 2018. Pore-scale analyses of heterogeneity and representative elementary volume for unconventional shale rocks using statistical tools. J. Pet. Explor. Prod. Technol. 8, 753–765. https://doi.org/10.1007/s13202-017-0377-4.

Bazaikin, Y., Gurevich, B., Iglauer, S., Khachkova, T., Kolyukhin, D., Lebedev, M., Lisitsa, V., Reshetova, G., 2017. Effect of CT image size and resolution on the accuracy of rock property estimates. J. Geophys. Res. Solid Earth 122, 3635–3647. https://doi.org/10.1002/2016JB013575.

Bear, Jacob, 1972. Dynamics of Fluids in Porous Media. Dover Publications, New York.

Bernabé, Y., Li, M., Maineult, A., 2010. Permeability and pore connectivity: a new model based on network simulations. J. Geophys. Res. Solid Earth 115. https://doi.org/10.1029/2010JB007444.

Blunt, M.J., Bijeljic, B., Dong, H., Gharbi, O., Iglauer, S., Mostaghimi, P., Paluszny, A., Pentland, C., 2013. Pore-scale imaging and modelling. Adv. Water Resour. 51, 197–216. https://doi.org/10.1016/j.advwatres.2012.03.003.

Civan, F., 2002. Relating permeability to pore connectivity using A power-law flow unit equation. Petrophysics - The SPWLA Journal of Formation Evaluation and Reservoir Description 43.

Comisky, J.T., Newsham, K.E., Rushing, J.A., Blasingame, T.A., 2007. A comparative study of capillary-pressure-based empirical models for estimating absolute permeability in tight gas sands. Presented at the SPE Annual Technical Conference and Exhibition. https://doi.org/10.2118/110050-MS. SPE-110050-MS.

Darcy, H., 1856. In: Dalmont, V., Ed (Eds.), Les Fontaines Publiques de la Ville de Dijon. Exposition et Application des Principes a Suivre et des Formulesa Employer dans les Questions de Distribution d'Eau, Paris, p. 647.

Dasgupta, T., Mukherjee, S., 2020. Porosity in carbonates. In: Dasgupta, T., Mukherjee, S. (Eds.), Sediment Compaction and Applications in Petroleum Geoscience. Springer International Publishing, Cham, pp. 9–18. https://doi.org/10.1007/978-3-030-13442-6_2.

Dastidar, R., Sondergeld, C.H., Rai, C.S., 2007a. An improved empirical permeability estimator from mercury injection for tight clastic rocks. Petrophysics - The SPWLA Journal of Formation Evaluation and Reservoir Description 48.

Devarapalli, R.S., Islam, A., Faisal, T.F., Sassi, M., Jouiad, M., 2017. Micro-CT and FIB–SEM imaging and pore structure characterization of dolomite rock at multiple scales. Arabian J. Geosci. 10, 361. https://doi.org/10.1007/s12517-017-3120-z.

Ebrahimi, P., Vilcáez, J., 2019. Transport of barium in fractured dolomite and sandstone saline aquifers. Sci. Total Environ. 647, 323–333. https://doi.org/10.1016/j.scitotenv.2018.08.008.

Ghanbarian, B., 2022. Estimating the scale dependence of permeability at pore and core scales: incorporating effects of porosity and finite size. Adv. Water Resour. 161, 104123 https://doi.org/10.1016/j.advwatres.2022.104123.

Gostick, J.T., 2017. Versatile and efficient pore network extraction method using marker-based watershed segmentation. Phys. Rev. E 96 (2–1), 023307. https://doi.org/10.1103/PhysRevE.96.023307.

Hollis, C., 2011. Diagenetic controls on reservoir properties of carbonate successions within the Albian–Turonian of the Arabian Plate. Petrol. Geosci. 17, 223–241. https://doi.org/10.1144/1354-079310-032.

Ishola, O., Vilcáez, J., 2022. Machine learning modeling of permeability in 3D heterogeneous porous media using a novel stochastic pore-scale simulation approach. Fuel 321, 124044. https://doi.org/10.1016/j.fuel.2022.124044.

Ishola, O., Alexander, A., Vilcáez, J., 2022. Statistical and neural network analysis of the relationship between the stochastic nature of pore connectivity and flow properties of heterogeneous rocks. J. Nat. Gas Sci. Eng. 105, 104719 https://doi.org/10.1016/j.jngse.2022.104719.

Jivkov, A.P., Xiong, Q., 2014. A network model for diffusion in media with partially resolvable pore space characteristics. Transport Porous Media 105, 83–104. https://doi.org/10.1007/s11242-014-0360-1.

Jivkov, A.P., Hollis, C., Etiese, F., McDonald, S.A., Withers, P.J., 2013. A novel architecture for pore network modelling with applications to permeability of porous media. J. Hydrol. 486, 246–258. https://doi.org/10.1016/j.jhydrol.2013.01.045.

Kamath, J., 1992a. Evaluation of accuracy of estimating air permeability from mercury-injection data. SPE Form. Eval. 7, 304–310. https://doi.org/10.2118/18181-PA.

Khirevich, S., Ginzburg, I., Tallarek, U., 2015. Coarse- and fine-grid numerical behavior of MRT/TRT lattice-Boltzmann schemes in regular and random sphere packings. J. Comput. Phys. 281, 708–742. https://doi.org/10.1016/j.jcp.2014.10.038.

Kolodzie Jr., S., 1980a. Analysis of pore throat size and use of the waxman-smits equation to determine OOIP in spindle field, Colorado. Presented at the SPE Annual Technical Conference and Exhibition. https://doi.org/10.2118/9382-MS. SPE-9382-MS.

Malin, P.E., Leary, P.C., Cathles, L.M., Barton, C.C., 2020. Observational and critical state physics descriptions of long-range flow structures. Geosciences 10. https://doi.org/10.3390/geosciences10020050.

Mees, F., Swennen, R., Geet, M. Van, Jacobs, P., 2003. Applications of X-Ray Computed Tomography in the Geosciences, vol. 215. Geological Society, London, Special Publications, pp. 1–6. https://doi.org/10.1144/GSL.SP.2003.215.01.01.

Mehmani, A., Prodanović, M., 2014. The effect of microporosity on transport properties in porous media. Adv. Water Resour. 63, 104–119. https://doi.org/10.1016/j.advwatres.2013.10.009.

Morad, S., Al-Ramadan, K., Ketzer, J.M., De Ros, L.F., 2010. The impact of diagenesis on the heterogeneity of sandstone reservoirs: a review of the role of depositional facies and sequence stratigraphy. AAPG (Am. Assoc. Pet. Geol.) Bull. 94, 1267–1309. https://doi.org/10.1306/04211009178.

Moslemipour, A., Sadeghnejad, S., 2021. Dual-scale pore network reconstruction of vugular carbonates using multi-scale imaging techniques. Adv. Water Resour. 147, 103795 https://doi.org/10.1016/j.advwatres.2020.103795.

Okabe, H., Blunt, M.J., 2004. Prediction of permeability for porous media reconstructed using multiple-point statistics. Phys. Rev. E 70, 066135. https://doi.org/10.1103/PhysRevE.70.066135.

Omar, K., Vilcáez, J., 2022. Removal of toxic metals from petroleum produced water by dolomite filtration. J. Water Proc. Eng. 47, 102682 https://doi.org/10.1016/j.jwpe.2022.102682.

Oostrom, M., Mehmani, Y., Romero-Gomez, P., Tang, Y., Liu, H., Yoon, H., Kang, Q., Joekar-Niasar, V., Balhoff, M.T., Dewers, T., Tartakovsky, G.D., Leist, E.A., Hess, N. J., Perkins, W.A., Rakowski, C.L., Richmond, M.C., Serkowski, J.A., Werth, C.J., Valocchi, A.J., Wietsma, T.W., Zhang, C., 2016. Pore-scale and continuum simulations of solute transport micromodel benchmark experiments. Comput. Geosci. 20, 857–879. https://doi.org/10.1007/s10596-014-9424-0.

Petrovskyy, D., Van Dijke, M.I.J., Jiang, Z., Geiger, S., 2021. Phase connectivity in pore-network models for capillary-driven flow. Adv. Water Resour. 147, 103776 https://doi.org/10.1016/j.advwatres.2020.103776.

Regnet, J.B., David, C., Robion, P., Menéndez, B., 2019. Microstructures and physical properties in carbonate rocks: a comprehensive review. Mar. Petrol. Geol. 103, 366–376. https://doi.org/10.1016/j.marpetgeo.2019.02.022.

Reinhardt, M., Jacob, A., Sadeghnejad, S., Cappuccio, F., Arnold, P., Frank, S., Enzmann, F., Kersten, M., 2022. Benchmarking conventional and machine learning segmentation techniques for digital rock physics analysis of fractured rocks. Environ. Earth Sci. 81, 71. https://doi.org/10.1007/s12665-021-10133-7.

Sadeghnejad, S., Reinhardt, M., Enzmann, F., Arnold, P., Brandstätter, B., Ott, H., Wilde, F., Hupfer, S., Schäfer, T., Kersten, M., 2023. Minkowski functional evaluation of representative elementary volume of rock microtomography images at multiple resolutions. Adv. Water Resour. 179, 104501 https://doi.org/10.1016/j.advwatres.2023.104501.

Sahin, A., Ali, A.Z., Saner, S., Menouar, H., 2007. Permeability anisotropy distributions in an upper jurassic carbonate reservoir, eastern Saudi Arabia. J. Petrol. Geol. 30, 147–158. https://doi.org/10.1111/j.1747-5457.2007.00147.x.

Saraji, S., Piri, M., 2015. The representative sample size in shale oil rocks and nano-scale characterization of transport properties. Int. J. Coal Geol. 146, 42–54. https://doi.org/10.1016/j.coal.2015.04.005.

Saxena, N., Hows, A., Hofmann, R., O. Alpak, F., Freeman, J., Hunter, S., Appel, M., 2018. Imaging and computational considerations for image computed permeability: operating envelope of Digital Rock Physics. Adv. Water Resour. 116, 127–144. https://doi.org/10.1016/j.advwatres.2018.04.001.

Shabani, B., Vilcáez, J., 2019. TOUGHREACT-CO2Bio – a new module to simulate geological carbon storage under biotic conditions (Part 1): the multiphase flow of CO2-CH4-H2-H2S gas mixtures. J. Nat. Gas Sci. Eng. 63, 85–94. https://doi.org/10.1016/j.jngse.2019.01.013.

Shabani, B., Pashin, J., Vilcáez, J., 2020. TOUGHREACT-CO2Bio – a new module to simulate geological carbon storage under biotic conditions (Part 2): the bio-geochemical reactive transport of CO2-CH4-H2-H2S gas mixtures. J. Nat. Gas Sci. Eng. 76, 103190 https://doi.org/10.1016/j.jngse.2020.103190.

Starnoni, M., Pokrajac, D., Neilson, J.E., 2017. Computation of fluid flow and pore-space properties estimation on micro-CT images of rock samples. Comput. Geosci. 106, 118–129. https://doi.org/10.1016/j.cageo.2017.06.009.

Sun, J., Dong, H., Arif, M., Yu, L., Zhang, Y., Golsanami, N., Yan, W., 2021. Influence of pore structural properties on gas hydrate saturation and permeability: a coupled pore-scale modelling and X-ray computed tomography method. J. Nat. Gas Sci. Eng. 88, 103805 https://doi.org/10.1016/j.jngse.2021.103805.

Swanson, B.F., 1981. A simple correlation between permeabilities and mercury capillary pressures. J. Petrol. Technol. 33, 2498–2504. https://doi.org/10.2118/8234-PA.

Uchic, M.D., Holzer, L., Inkson, B.J., Principe, E.L., Munroe, P., 2007. Three-dimensional microstructural characterization using focused ion beam tomography. MRS Bull. 32, 408–416. https://doi.org/10.1557/mrs2007.64.

Vilcáez, J., 2020. Reactive transport modeling of produced water disposal into dolomite saline aquifers: controls of barium transport. J. Contam. Hydrol. 233, 103600 https://doi.org/10.1016/j.jconhyd.2020.103600.

Vilcáez, J., Morad, S., Shikazono, N., 2017. Pore-scale simulation of transport properties of carbonate rocks using FIB-SEM 3D microstructure: implications for field scale solute transport simulations. J. Nat. Gas Sci. Eng. 42, 13–22. https://doi.org/10.1016/j.jngse.2017.02.044.

Wang, Y., Miller, J.D., 2020. Current developments and applications of micro-CT for the 3D analysis of multiphase mineral systems in geometallurgy. Earth Sci. Rev. 211 https://doi.org/10.1016/j.earscirev.2020.103406.

Wang, G., Chang, X., Yin, W., Li, Y., Song, T., 2017. Impact of diagenesis on reservoir quality and heterogeneity of the Upper Triassic Chang 8 tight oil sandstones in the Zhenjing area, Ordos Basin, China. Mar. Petrol. Geol. 83, 84–96. https://doi.org/10.1016/j.marpetgeo.2017.03.008.

Wells, J.D., Amaefule, J.O., 1985. Capillary pressure and permeability relationships in tight gas sands. Presented at the SPE/DOE Low Permeability Gas Reservoirs Symposium. https://doi.org/10.2118/13879-MS. SPE-13879-MS.

Wells, J., Amaefule, J., 1985. Capillary pressure and permeability relationships in tight gas sands. SPE/DOE Low Permeability Gas Reservoirs Symposium.

Westphal, H., Surholt, I., Kiesl, C., Thern, H.F., Kruspe, T., 2005. NMR measurements in carbonate rocks: problems and an approach to a solution. Pure Appl. Geophys. 162, 549–570. https://doi.org/10.1007/s00024-004-2621-3.

Willson, C.S., Lu, N., Likos, W.J., 2012. Quantification of grain, pore, and fluid microstructure of unsaturated sand from X-ray computed tomography images. Geotech. Test J. 35, 20120075.

Wu, Y., Lin, C., Ren, L., Yan, W., An, S., Chen, B., Wang, Y., Zhang, X., You, C., Zhang, Y., 2018. Reconstruction of 3D porous media using multiple-point statistics based on a 3D training image. J. Nat. Gas Sci. Eng. 51, 129–140. https://doi.org/10.1016/j.jngse.2017.12.032.

Xiong, Q., Baychev, T.G., Jivkov, A.P., 2016. Review of pore network modelling of porous media: experimental characterisations, network constructions and applications to reactive transport. J. Contam. Hydrol. 192, 101–117. https://doi.org/10.1016/j.jconhyd.2016.07.002.

Yang, Y., Aplin, A.C., 2010. A permeability–porosity relationship for mudstones. Mar. Petrol. Geol. 27, 1692–1697. https://doi.org/10.1016/j.marpetgeo.2009.07.001.

Yang, X., Scheibe, T.D., Richmond, M.C., Perkins, W.A., Vogt, S.J., Codd, S.L., Seymour, J.D., McKinley, M.I., 2013. Direct numerical simulation of pore-scale flow in a bead pack: comparison with magnetic resonance imaging observations. Adv. Water Resour. 54, 228–241. https://doi.org/10.1016/j.advwatres.2013.01.009.

Yang, X., Mehmani, Y., Perkins, W.A., Pasquali, A., Schönherr, M., Kim, K., Perego, M., Parks, M.L., Trask, N., Balhoff, M.T., Richmond, M.C., Geier, M., Krafczyk, M., Luo, L.-S., Tartakovsky, A.M., Scheibe, T.D., 2016. Intercomparison of 3D pore-scale flow and solute transport simulation methods. Adv. Water Resour. 95, 176–189. https://doi.org/10.1016/j.advwatres.2015.09.015.

Zhang, Shuo, Lu, Peng, Dave, Cantrell, Yan, Zaretskiy, Dawn, Jobe, Agar, Susan M., 2018. Improved quantification of the porosity–permeability relationship of limestones using petrographical texture. Petrol. Geosci. 24, 440–448. https://doi.org/10.1144/petgeo2017-052.

Zhang, P., Lee, Y.I., Zhang, J., 2019. A review of high-resolution X-ray computed tomography applied to petroleum geology and a case study. Micron 124, 102702. https://doi.org/10.1016/j.micron.2019.102702.

Zhang, K., Wang, S., Wang, L., Cheng, Y., Li, W., Han, X., Liu, C., Su, H., 2022. 3D visualization of tectonic coal microstructure and quantitative characterization on topological connectivity of pore-fracture networks by Micro-CT. J. Petrol. Sci. Eng. 208, 109675 https://doi.org/10.1016/j.petrol.2021.109675.